

Bimetallic Selenide CuFeSe₂ as Mg-Storage Material for Rechargeable Magnesium Batteries

Qinghong Kong^{+[a]}, Lianmeng Cui^{+[a]}, Xiaobin Liao,^[a] Ruohan Yu,^[a] Yalong Jiang,^[c] Junjun Wang,^[a] Wenwei Zhang,^[a] Yu Wang,^[a] Lei Zhang,^{*[a, b]} and Qinyou An^{*[a, b]}

Rechargeable magnesium batteries (RMBs) are appealing alternatives for energy storage systems based on the high theoretical capacity, low price and high security of the Mg metal anode. Nevertheless, the shortage of high-performance cathode materials severely obstructs its development. As an important conversion material, transition metal selenides, with desirable theoretical capacity and weak bond energy (Mg–Se), have attracted more attention in recent years. In this study, CuFeSe₂ (CFS) nanoparticles were produced by a hydrothermal approach and its feasibility as a cathode material for RMBs was further investigated. Given the synergistic effect between Cu

and Fe, the optimized CFS shows a reversible capacity of 120 mAh g⁻¹ at 100 mA g⁻¹, outstanding long-term cyclability (86 mAh g⁻¹ at 1 A g⁻¹ after 600 cycles), and prominent rate capability (85 mAh g⁻¹ at 1 A g⁻¹). Density functional theory (DFT) computations conclude CFS exhibits a suitable migration barrier for Mg²⁺ along the tunnel of 0.92 eV. An in-depth investigation of the mechanism demonstrates that the Mg storage process can be divided into solid solution reaction and the conversion processes by *ex-situ* techniques. This work contributes to further investigate the Mg²⁺ storage mechanism of cathode materials for RMBs.

1. Introduction

Lithium-ion batteries (LIBs) have attracted extensive attention for use in electric-powered vehicles, wearable devices and many other aspects due to their high energy density and long cycling life during the past decades.^[1–5] However, the shortage of lithium resources supply, the possibility of further rise in price and security concerns restrict the sustainable development of LIBs.^[6,7] Rechargeable magnesium batteries (RMBs), as a significant multivalent metal-ion batteries, received extensive concern in the near future owing to their high theoretical volumetric capacity (3833 mAh cm⁻³ for Mg vs. 2062 mAh cm⁻³ for Li), abundant natural resources (2% of the earth's crust element content for Mg vs. only 0.002% for Li), low reduction

potential (−2.37 V vs. SHE), and without the dendrite formation of magnesium metal anode in most cases.^[8–11]

Although these are satisfactory merits, many challenges still remain in RMBs. One of the prominent difficulties facing the RMBs is the strong Coulombic interaction between divalent Mg²⁺ and the anions of the cathode materials, which results in the sluggish diffusion kinetics of Mg²⁺ ions.^[9,12,13] Based on the consideration of the abovementioned issue, an increasing number of suitable cathode materials for RMBs have been investigated at present, such as transition metal oxides (V₂O₅,^[14,15] MnO₂,^[16] MoO₃,^[17] TiO₂^[18–20]), transition metal sulfides (CoS,^[12] Co₂S,^[21] CuS,^[22–25] VS₄^[26]), transition metal selenides (CuSe,^[27–29] WSe₂,^[30] TiSe₂^[31]), polyanionic compounds (Li₃V₂(PO₄)₃^[32]), and so on. Nevertheless, most metal oxides and polyanionic compounds electrode materials are mismatch with Mg anode for the strong interaction between Mg²⁺ and O²⁻.^[33] Hence, discovering and exploring promising transition metal chalcogenides as Mg-storage materials with excellent cyclic stability and high specific capacity is necessary. In comparison with sulfur elements in the same main group, selenium compounds have a higher electronic conductivity (1×10⁻³ S m⁻¹ for Se vs. 5×10⁻²⁸ S m⁻¹ for S),^[34] lower electronegativity and the special electron orbital mixing effects between Se 3d and transition metal M 4p.^[35,36] Besides, depending upon the hard and soft acids and bases theory,^[37–39] the soft Se²⁻ anion could weaken the interaction with Mg²⁺ cations (hard acid), which is advantageous to promote the Mg-storage reaction reversibility.

Therefore, the transition metal selenides are suitable cathode materials for RMBs. Zhang *et al.* reported NiCo₂Se₄ nanosheets (NCS-S), which has a satisfactory capacity of 145 mAh g⁻¹ and remains a discharge capacity of 40 mAh g⁻¹ after 1000 cycles at 500 mA g⁻¹. The higher specific surface area of NCS-S helps to promote the diffusion process of Mg²⁺, and its unique layered microflower structure is beneficial to

[a] Q. Kong,^{+[a]} L. Cui,^{+[a]} X. Liao, R. Yu, J. Wang, W. Zhang, Y. Wang, L. Zhang, Q. An
State Key Laboratory of Advanced Technology for Materials Synthesis and Processing
International School of Materials Science and Engineering
Wuhan University of Technology
Wuhan, 430070, Hubei, P. R. China
E-mail: zhanglei1990@whut.edu.cn

[b] L. Zhang, Q. An
Sanya Science and Education Innovation Park
Wuhan University of Technology
Sanya, 572000, Hainan, P. R. China
E-mail: anqinyou86@whut.edu.cn

[c] Y. Jiang
State Key Laboratory of New Textile Materials and Advanced Processing Technologies
Wuhan Textile University
Wuhan, 430200, Hubei, P. R. China

[+] These authors contribute equally to this work.

Supporting information for this article is available on the WWW under
<https://doi.org/10.1002/batt.202400055>

maintaining structural integrity and enhancing cyclic stability.^[40] Furthermore, Zhou *et al.* synthesized $\text{Ni}_{0.75}\text{Fe}_{0.25}\text{Se}_2$ (NFS) micro-flowers through the Fe doped into NiSe_2 by solvothermal method. Due to the bimetallic cooperative effect, NFS displays more redox active sites and faster Mg^{2+} diffusion kinetics than binary metal chalcogenides with a long lifespan (148 mAh g^{-1} after 500 cycles at 20 mA g^{-1}) and high reversible capacity (190 mAh g^{-1}).^[41] Nonetheless, the above work still exists the shortcoming of lower capacity at a high current density and the mechanism of brilliant Mg-storage performance still needs to be further explored. Consequently, developing transition metal selenides materials with excellent electrochemical properties is an indispensable part of RMBs.

In this work, we synthesized copper-iron bimetallic selenides CuFeSe_2 (CFS, for short) by one-step hydrothermal method as cathode materials to explore its ability to store magnesium ions for RMBs, tested electrochemical performance, and investigated its magnesium storage mechanism for the first time. Benefiting from bimetallic synergy effects and self-generated metallic Fe during cycling, the CFS exhibits remarkable long-term cyclability over 600 cycles with a maximum capacity of 105 mAh g^{-1} at 1.0 A g^{-1} , excellent rate capability of 85 mAh g^{-1} at 1 A g^{-1} , and reversible discharge capacity of 120 mAh g^{-1} at 100 mA g^{-1} . An

in-depth kinetic investigation indicates that the capacitive-controlling contribution reached 92.6% at 1.5 mV s^{-1} , illustrating that the storage behavior of CFS is primarily dominated by the capacitive process. The spin-polarized density functional theory (DFT) simulations were performed to examine the energy barrier for transferring Mg^{2+} in the tunnel structure. Moreover, the Mg-storage mechanism was demonstrated by *ex-situ* X-ray diffraction (XRD), *ex-situ* X-ray photoelectron spectroscopy (XPS), and *ex-situ* high-resolution TEM (HRTEM). Time-of-flight-secondary ion mass spectrometry (TOF-SIMS) and XPS were investigated to further indicate the intercalation of Mg^{2+} into CFS. Subsequently, when applied CFS electrode to hybrid $\text{Mg}^{2+}/\text{Li}^+$ batteries (MLIBs), it exhibits superior ultra-long lifespan and high cycling stability with a capacity retention of 87.6% after 9500 cycles at 3000 mA g^{-1} .

2. Results and Discussion

As illustrated in Figure 1a, the CFS samples are prepared by a facile and rapid hydrothermal process. The crystal structure of CFS was studied via powder XRD analysis, and the XRD pattern (Figure 1b) is well indexed to the tetragonal phase CuFeSe_2 (space

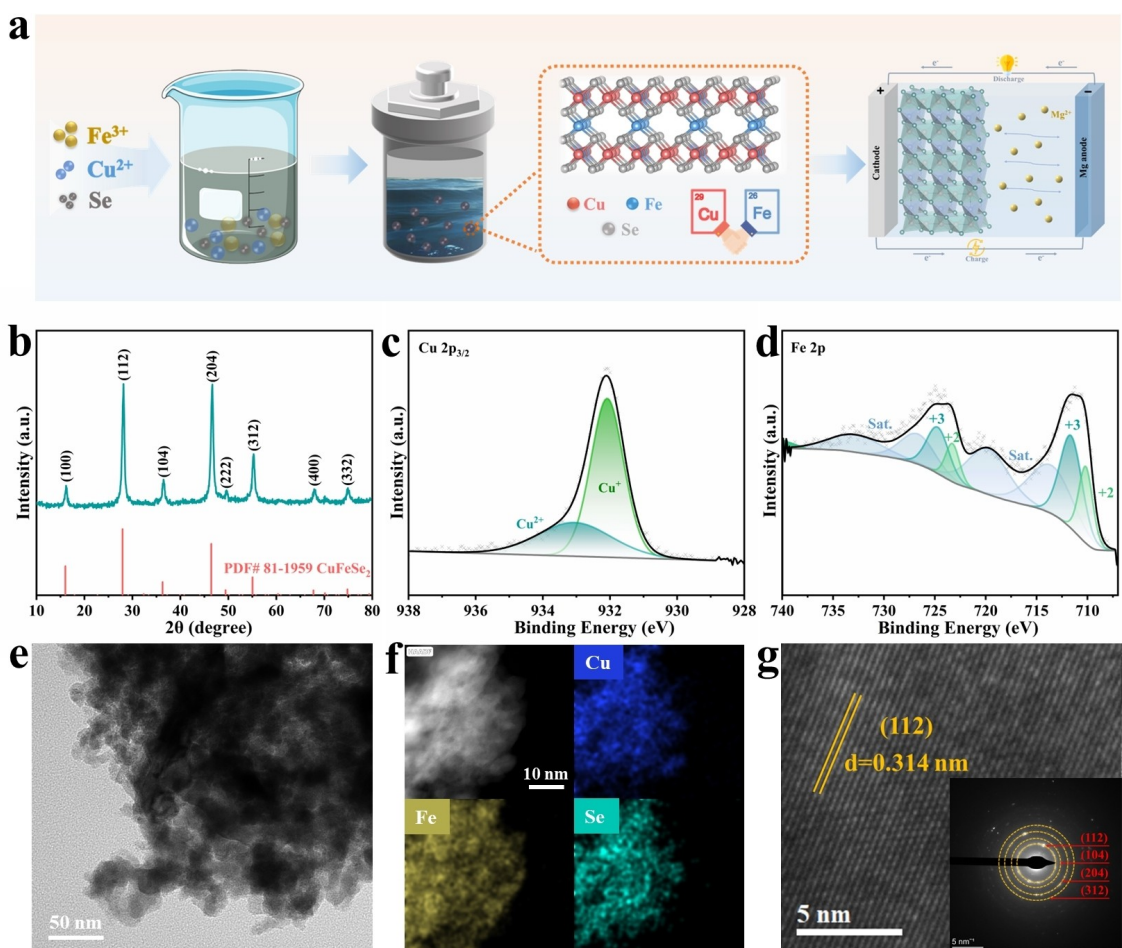


Figure 1. Structural analysis and morphology characterization. (a) Schematic for the preparation of CFS. (b) XRD pattern, (c) XPS spectrum of $\text{Cu } 2\text{p}_{3/2}$ and (d) $\text{Fe } 2\text{p}$, (e) TEM image, (f) HAADF image and EDS elemental mappings, (g) HRTEM image (inset displaying the corresponding SAED) of as-synthesized CFS.

group: $P-42c$) with $a=b=5.53\text{ \AA}$ and $c=11.049\text{ \AA}$ (PDF#81-1959). The sharp diffraction peaks without other distinct impurity peaks are detected, indicating that well-crystallized and highly purified samples were synthesized successfully.

The XPS spectrum in Figure S1a confirms that the signals of Cu, Fe and Se are visible by the survey spectrum. Additionally, the valences analysis of different elements was conducted using the high-resolution XPS spectra. Two characteristic peaks can be respectively detected at 932.1 and 933.1 eV, affirming the existence of Cu^+ and Cu^{2+} in Cu $2p_{3/2}$ XPS spectra (Figure 1c). The primary peaks at 724.9 eV and 711.8 eV can be ascribed to $2p_{1/2}$ and $2p_{3/2}$ of Fe^{3+} species with a binding energy splitting of 13.1 eV, two main peaks at 723.4 eV and 710.2 are derived from Fe $2p_{1/2}$ and Fe $2p_{3/2}$ of Fe^{2+} . The satellite peaks of Fe 2p obtained at 714.0, 720.0, 727.0, and 733.4 eV can be seen clearly in Figure 1d. The Se $3d_{5/2}$ and $3d_{3/2}$ peaks respectively are confirmed at 57.4 eV and 58.4 eV, as displayed in the Se 3d XPS spectrum (Figure S1b), which is agreement with that of Se^{2-} . The atomic absorption spectroscopy (AAS) test was used to quantitatively analyze given elements to determine the proportion of different elements in synthetic materials. As illustrated in Table S1, the Cu, Fe, and Se atomic ratios are 1.06:1:1.94, approaching the stoichiometric ratio of 1:1:2, which can be consistent well with the XRD pattern.

Figure S2 and Figure 1e show the SEM and HAADF images of the CFS, indicating that CFS is mainly made up of nanoparticles smaller than 50 nm in size, together with a small quantity of nanosheets. This composition is conducive to increasing the contact surface of electrode/electrolyte and shortening the magnesium ions diffusion path. Additionally, it is evident from the EDS elemental mapping images (Figure S3) that Cu, Fe, and Se elements are equally distributed. The TEM elemental mapping images (Figure 1f) can also further illustrate the uniform distribution of constituent elements. The interplanar spacing of material obtained by high-resolution TEM is 0.314 nm in Figure 1g, belonged to the (112) crystal plane of as-obtained CFS materials. The selected area electron diffraction (SAED) pattern (shown inset in Figure 1g) depicts several distinct concentric circles with bright diffraction spots, which means good crystallinity and could be indexed to (112), (104), (204), and (312) crystal planes of CFS samples. Given all that, CuFeSe_2 materials were prepared successfully in the face of all this.

The electrochemical magnesium storage properties were studied by assembling coin cells in all phenyl complex $[(\text{MgPhCl})_2\text{-AlCl}_3\text{/THF, APC}]$ electrolyte with a Mg foil anode. The compatibility between the APC electrolyte and Mg anode was characterized by the CV profile in Figure S4, which shows excellent stability and high Mg stripping/plating efficiency below 2.8 V, and demonstrates that the APC electrolyte is accessible within 0.1–2.1 V. Figure 2a displays the typical CV curves of CFS, in the anodic scan process, two oxidation peaks are visible at approximately 1.8 and 1.5 V respectively. Besides the first cycle, a weak reduction peak appearing at 1.3 V could be attributed to the insertion of Mg^{2+} resulting in partial CuFeSe_2 transform into $\text{Mg}_x\text{CuFeSe}_2$, another distinct peak at about 0.9 V could be explained by $\text{Mg}_x\text{CuFeSe}_2$ reduce to Cu_2Se and Fe^0 in the second cycle. The activation process is the chief cause of these two reduction peaks diverting

to a higher voltage in the subsequent cycles.^[42] The first cycle curve differs from the following cycles can be attributed to the side reactions between electrolyte and metal anode, and the activation process of CuFeSe_2 cathode.^[43–46] The reduction peaks of different cycles almost overlapped except for the first cycle, suggesting CFS cathode materials with stable electrochemical properties and favorable reversibility. Two obvious discharge voltage plateaus can be observed in Figure 2b, one with a higher slope at 1.3 V and the other with a gentle plateau at 0.9 V beginning with the second cycle, indicating a two-step reaction progress, such results are compatible with the CV data. And CFS achieved an initial discharge capacity of 270 mAh g^{-1} , while only a relatively low capacity of 95 mAh g^{-1} at fully charged state. After the 30th cycle, the discharge and charge capacities respectively are 124 and 151 mAh g^{-1} , with a Coulombic efficiency of 82%. Such a low initial Columbic efficiency may be attributable to electrode activation in the first few cycles.

As given in Figure 2c, the discharge capacities of CFS are measured to be 120, 118, 116, 113, 107, and 85 mAh g^{-1} at 100, 200, 300, 500, and 1000 mAh g^{-1} in turn. Afterwards, when returning to 100 mAh g^{-1} , CFS displays a specific capacity of 128 mAh g^{-1} , which is higher than that at the initial stage of 100 mAh g^{-1} . This phenomenon may be ascribed to the continuous activation process results in the production of more active sites during the cycling process. In addition, the gradual penetration of the electrolyte into the electrode material will also contribute to an increase in specific capacity.^[42,45,47] Therefore, CFS exhibits excellent reversibility and remarkable rate capability ranging from 100 to 1000 mAh g^{-1} . The rate capability of CFS is compared with several representative cathodes in Figure S6, and CFS exhibits a better rate capability than most typical cathodes, demonstrating the advantages of bimetal selenides in Mg-storage. Moreover, the CFS cathode presents fantastic long lifespan and high stability, as shown in Figure 2d. After ten activation cycles at a lower current density of 50 mA g^{-1} , the CFS electrode achieves a maximum discharge specific capacity of 105.4 mAh g^{-1} at 1000 mA g^{-1} and a reversible capacity of 85.6 mAh g^{-1} after 600 cycles. In addition, CFS also exhibits satisfactory cycling performance at 100 mA g^{-1} (Figure S5a) and 500 mA g^{-1} (Figure S5b). According to the aforementioned findings, the Coulombic efficiency is always greater than 98% at higher current densities compared to lower ones, which could be explained as the self-discharge phenomenon at a lower current density.^[26,48] Furthermore, the EIS analyses reveal superior long-life performance and rate capability, which indicate the charge transfer kinetics of the batteries. The Nyquist plots of the CFS electrodes at different states are depicted in Figure 2e. The charge transfer resistance (R_{ct}) of CFS before discharge, after 5 and 10 cycles is 1389, 30.97, and 55.59Ω , respectively. It is evident that the semicircle diameter sharply decreased upon the cycle of the CFS electrode, implying that CFS possesses a smaller charge-transfer resistance after cycling. The reasons for this phenomenon will be explained in the following content.

Further electrochemical kinetic analyses were conducted via CV test at multiple scan rates, presented in Figure 2f–2i. The CV curves at diverse scan rates exhibit a similar shape, as shown in

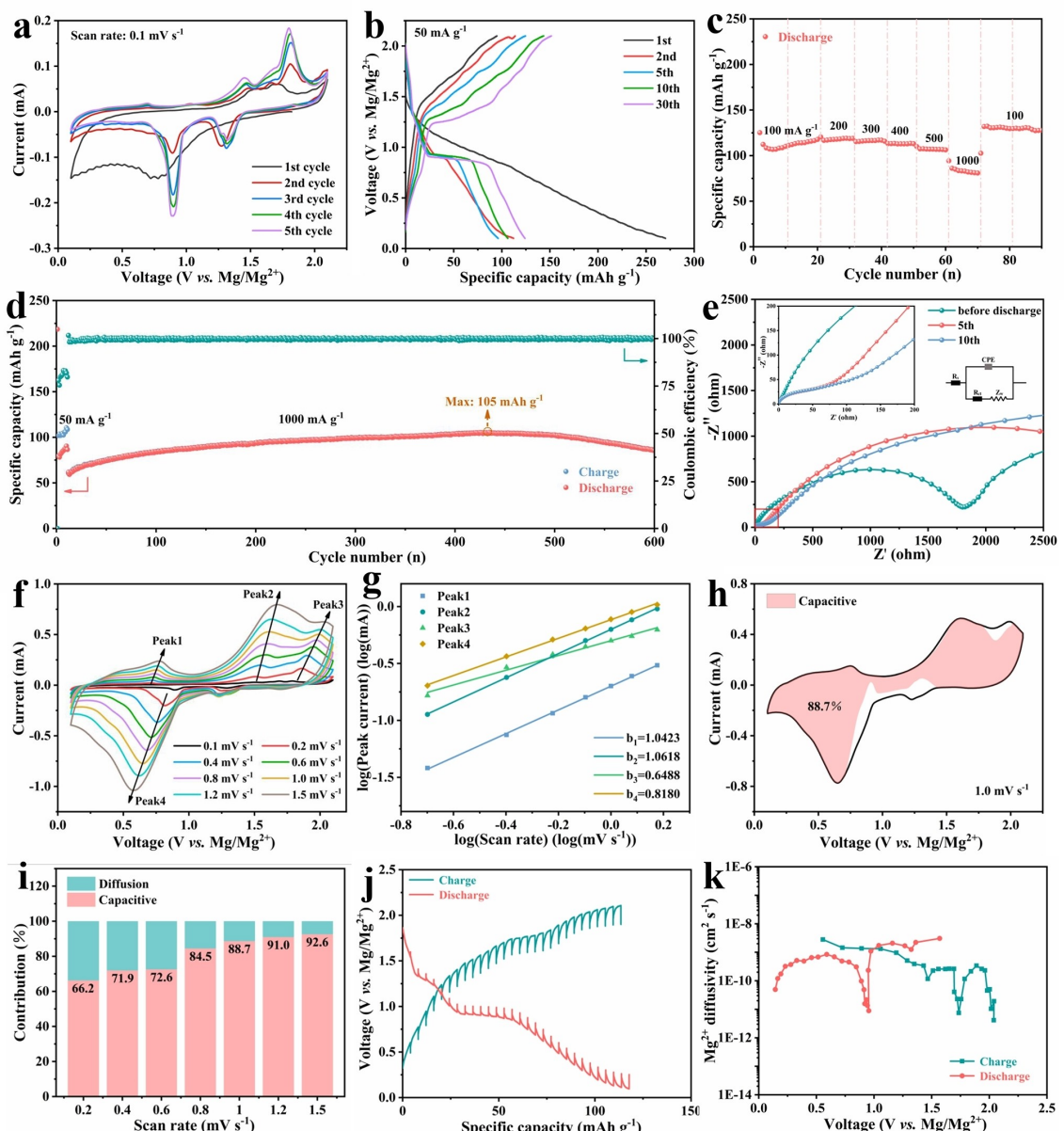


Figure 2. Electrochemical performance and kinetic analysis. (a) CV curves of the CFS electrode at a scan rate of 0.1 mV s^{-1} between 0.1 and $2.1 \text{ V vs. Mg/Mg}^{2+}$. (b) Galvanostatic charge-discharge curves of CFS at a current density of 50 mA g^{-1} . (c) Rate performance of CFS cathode at current rates from 100 to 1000 mA g^{-1} . (d) Long cycling performance at 1000 mA g^{-1} for 600 cycles. (e) Nyquist plots of CFS electrodes at different states, and inset is enlarged image of high frequency region and equivalent circuit. (f) CV curves of CFS electrode at various scan rates from 0.1 to 1.5 mV s^{-1} . (g) Corresponding log (peak current) vs. log (scan rate) plots of the redox peaks. (h) CV curves with capacitive-controlled contribution of CFS at 1.0 mV s^{-1} . (i) Corresponding capacitive-controlled contributions of CFS at various scan rates. (j) GITT test for CFS at current density of 50 mA g^{-1} and (k) corresponding calculated Mg^{2+} diffusion coefficients during charge and discharge process.

Figure 2f, indicating the excellent reversibility of CFS cathode materials. Based on the equation as follows: $i = av^b$, it can also be transformed into the $\log(i) = b\log(v) + \log(a)$, where a and b are changeable parameters, i is the peak current, and v is the scan rate. It is generally accepted that the electrochemical process is diffusion-controlled when the b value approaches 0.5, and the surface capacitive makes a major contribution when the b value is close to 1.0.^[49] As Figure 2g presents, the calculated b values from peak 1 to peak 4 are 1.0423, 1.0618, 0.6489, and 0.8180, respectively. Consequently, the electro-

chemical processes of CFS are mainly dominated by surface capacitance, which promotes the rapid conduction of ions. After that, the proportions of capacitive-controlled and diffusion-controlled were further analyzed by $i(V) = k_1v + k_2v^{1/2}$.^[50,51] Figure 2i and Figure S7 display the calculation results of capacitance and diffusion contribution of the CFS cathode. It can be seen that the capacitive contribution accounts for 66.2, 71.9, 72.6, 84.5, 88.7, 91.0, and 92.6% as the scan rate increases from 0.2 to 1.5 mV s^{-1} . The supremacy of the capacitance-controlled process should be accountable for the bimetallic strategy of

CFS, which is beneficial for promoting the rapid solid-state Mg^{2+} mobility and redox kinetics. Additionally, the galvanostatic intermittent titration technique (GITT) measurement was applied for the further analysis of the reaction kinetics of CFS cathode materials, and the following equation can calculate the Mg^{2+} diffusion coefficients (D^{GITT}):

$$D^{GITT} = \frac{4}{\pi\tau} \left(\frac{m_B V_M}{M_B S} \right)^2 \left(\frac{\Delta E_s}{\Delta E_c} \right)^2. \quad (1)$$

Figure 2k illustrates that the average Mg^{2+} diffusion coefficient on discharge and charge processes respectively are 7×10^{-10} and $4 \times 10^{-10} \text{ cm}^2 \text{s}^{-1}$, which is several orders of magnitude greater than other metal selenides previously reported, such as Cu_{2-x}Se ,^[43] CoSe_2 ,^[44,45] $\text{NiSe}_2\text{-CoSe}_2@\text{TiVCT}_x$,^[47] NiCo_2Se_4 ,^[40] and so on.

To further reveal the mechanism of magnesium-ion storage and the phase transformation of the CFS cathode during the electrochemical cycling processes, *ex-situ* XRD, SEM, XPS, TOF-SIMS, and HRTEM characterizations were carried out at fully discharged and charged states. The PTFE binder could be indexed to the sharp peak at 18.0° , which can be used to calibrate the XRD results in Figure 3a. There is no discernible diffraction peak shift at different discharge/charge states, which can be explained by Mg^{2+} insertion into the CFS lattice and is consistent with the electrochemical behavior observed in the CV test at 1.3 V. In addition, distinct peaks of Cu_2Se (PDF#88-2043) are identified at 27.1° and 45.0° , and signals at 32.8° could

be well-indexed to MgSe (PDF#65-2922) at initial discharged to 0.1 V. When first charging back to 2.1 V, there is a disappearance of Cu_2Se with the appearance of the CuSe (PDF#49-1757) at 31.1° . Still, the phase transformation process from Cu_2Se to CuSe is not presented at the following charge process. This is because a small amount of metallic Fe^0 generated at the first discharge process, and thus the excess Cu_2Se could be oxidized to CuSe . Figure 3b shows the HAADF images of the CFS cathode in the fully discharged state after 5 cycles, and the corresponding Se, Fe, Cu, Cl, and Mg elemental mappings are shown in Figure 3c-g, respectively. STEM mapping results deliver the heterogeneous Fe element distribution, demonstrating the formation of metal ferrum. Furthermore, the atomic picture (Figure 3i) can also certify this experimental result. Meanwhile, as shown in Figure S8, the heterogeneous distribution of Fe elements can also be observed in EDS elemental mappings of fully charged electrodes. *Ex-situ* XPS analyses of the cycled CFS cathodes at different states were performed to investigate the elemental valence changes and further demonstrate the existence of metallic Fe^0 . In the high-resolution Fe 2p spectra (Figure 3j), the peaks emerged at 708.0 eV and 721.2 eV of the fully-discharged state originated from $\text{Fe}^0 2p_{3/2}$ and $\text{Fe}^0 2p_{1/2}$, demonstrating the presence of metallic Fe. The weak Fe^0 peaks (707.9 eV and 721.1 eV) persist in the fully charged state. In addition, this phenomenon can also be observed in the Fe 2p spectra of the electrode after the first cycle and ten cycles (Figure S9), proving that Fe metal is generated in the initial stage of the electrochemical reaction. Therefore, we believe a

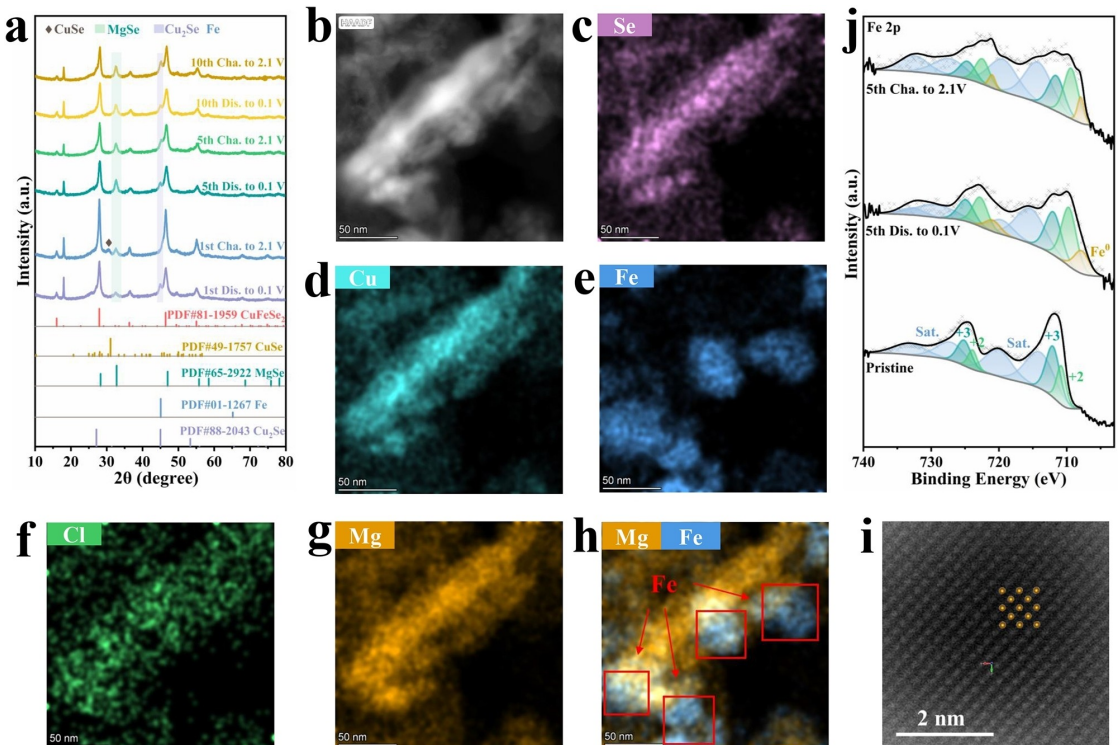


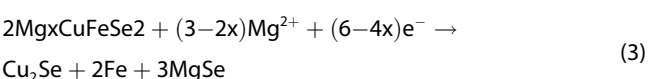
Figure 3. Structural changes of CFS during electrochemical reactions. (a) XRD patterns of the electrode at different states. (b) The HAADF images of the CFS cathode in the fully discharged state after 5 cycles and corresponding (c) Se (d) Fe (e) Cu (f) Cl and (g) Mg elemental mappings. (h) Distribution overlap diagram of Mg and Fe elements, and (i) the atomic phase diagram of Fe in the red box area. (j) XPS spectrum of Fe 2p at charge and discharge states after 5 cycles.

conversion reaction, generating the metallic iron, occurred during the discharge process. Metallic Fe exhibits good conductivity, making it function as an electrically conductive material, which is advantageous for the electrochemical performance of materials and explains the gradual decrease of charge-transfer resistance for the initial cycles.

The types of charge storage in CFS have also been studied. The intensity of Mg 1s peak varies significantly after the 5th charge and discharge process (Figure 4a). Meanwhile, the peak intensity of Cl⁻ remains almost unchanged and is very weak. This indicates that the intercalation ion is Mg²⁺ rather than MgCl⁺. The same results can also be observed in the electrode after the first and tenth cycles (Figure S11). Also, the results of TOF-SIMS measurements conducted at the first fully-discharged (Figure 4c) and fully-charged (Figure 4d) states suggest the same result as XPS. As shown in Figure 4c, Mg²⁺ content in the bulk phase changes significantly, indicating that most of the inserted Mg²⁺ has been removed during the charge process. Cl⁻ is predominantly distributed on the electrode surface, which may be caused by residual electrolyte. The *ex-situ* SEM analysis (Figure S12) shows similar changes in magnesium and chlorine content. Based on the XPS, SEM, and TOF-SIMS test results, we can conclude that in CFS, Mg²⁺ is the main energy storage ion.

The intrinsic properties and Mg²⁺ diffusion kinetics of the CFS were investigated via Density functional theory simulations. As displayed in Figure 4e and 4f, the fully relaxed CFS bulk exhibits the conductor-like projected density of states with a continuum

peak at the fermi level, proving the superior electronic conductivity of the CFS materials. According to the charge population analysis, the charges e⁻ are localized at the Se atom in the tunnel structure and manage the transfer behavior of Mg²⁺ along the tunnel. Whereafter, the energy barrier for transferring Mg²⁺ was clarified by the climbing image nudged elastic band method (CI-NEB). In Figure 4g, the CFS exhibits a migration barrier for Mg²⁺ along the c-axis is 0.92 eV, and the diffusion path diagram is shown in Figure S13. The diffusion energy barrier of Mg²⁺ along the b-axis is 0.80 eV, which can be seen from Figure S14. By comparing this result to other reported materials,^[52-54] this value is relatively appropriate and the insertion of magnesium ions can be carried out. Consequently, based on the aforementioned findings, we propose a two-step magnesium storage mechanism for CFS material. Based on the mentioned analyses and previous reports, the main discharge reactions can be briefly proposed as follows:



The electrochemical performance of CFS in the hybrid Mg²⁺/Li⁺ batteries were studied in a mixed-ion electrolyte (0.4 M APC + 1 M LiCl in THF). The initial five CV curves of CFS electrode in MLIBs scanning at 0.1 mVs⁻¹ can be seen in Figure 5a. With the exception of the initial cycle, the nearly overlapped CV curves in

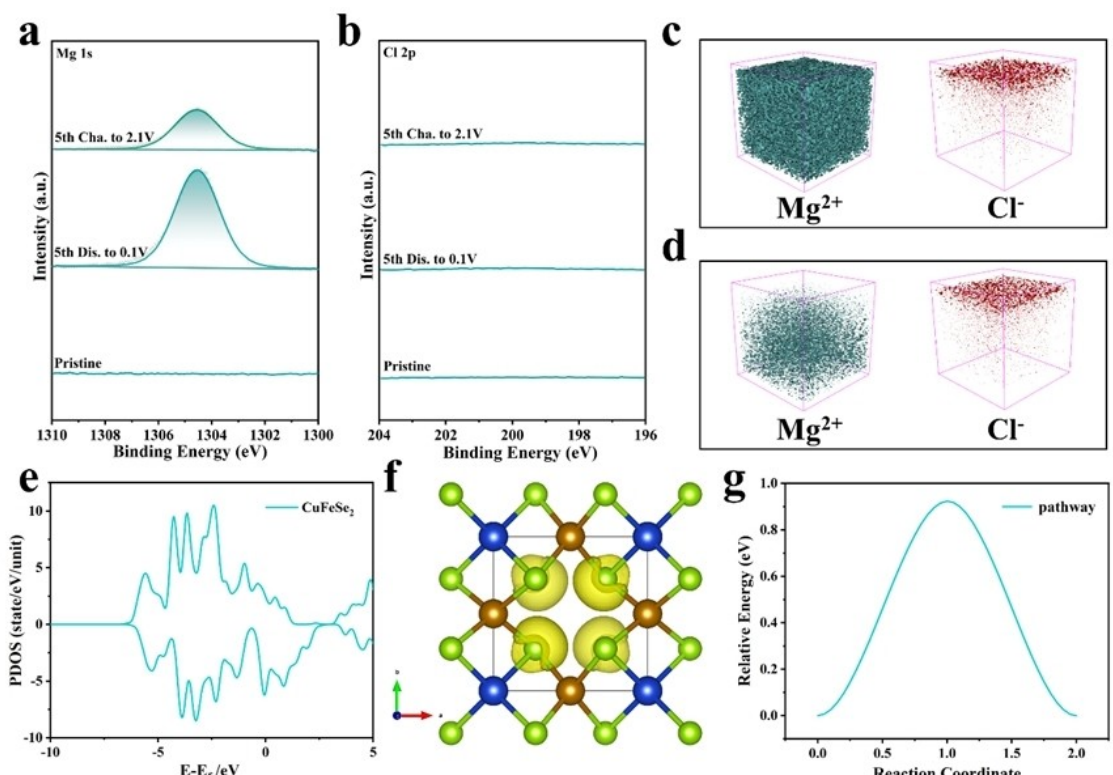


Figure 4. Magnesium storage mechanism of CFS. XPS spectrum of (a) Mg 1s and (b) Cl 2p at charge and discharge states after 5 cycles. TOF-SIMS 3D rendering models of Mg²⁺ and Cl⁻ at (c) discharge and (d) charge states after 5 cycles. (e) Density of states of CFS. (f) Charge population analysis of Se atoms in the tunnel structure and (g) energy barrier for transferring Mg²⁺ in the tunnel structure.

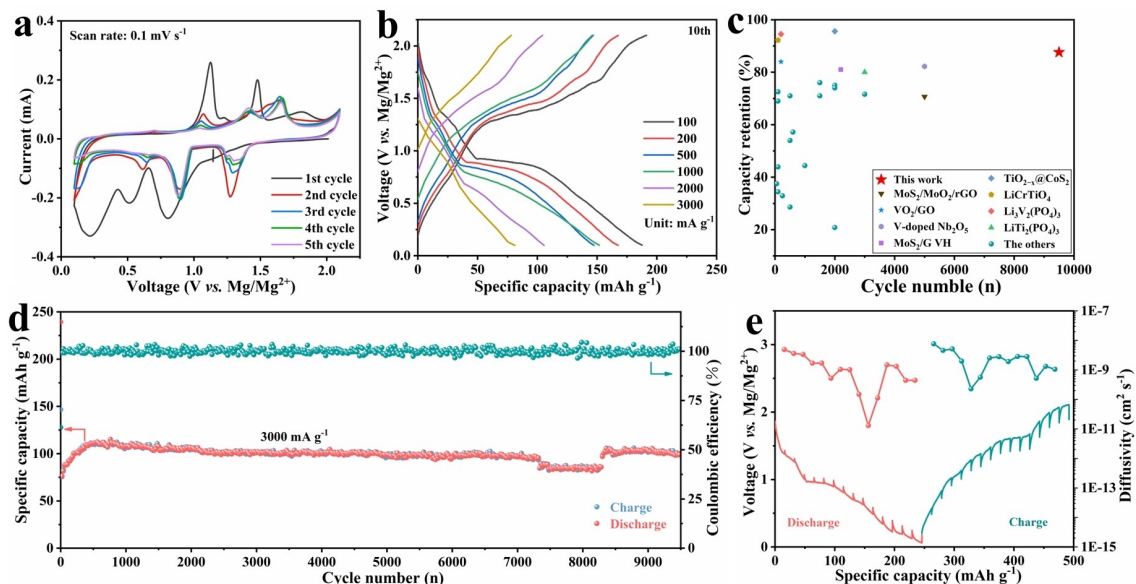


Figure 5. Electrochemical performance of CFS in MLIBs. (a) The CV curves of CFS at a scan rate of 0.1 mV s^{-1} . (b) Galvanostatic charge/discharge profiles of CFS at different current densities. (c) Comparation of the long cycling stability between CFS and reported materials for MLIBs. (d) Long-term cycling performance of CFS at 3000 mA g^{-1} . (e) GITT curve of CFS and diffusion coefficients during charge and discharge process.

the subsequent processes indicate the favorable electrochemical reversibility. The first cycle significantly differs from the others could be attributed to the irreversible reactions and the presence of surface oxidation layer of Mg anode.^[26,43,55] Moreover, there are two emerging peaks at 0.65 V and 1.1 V aside from the two pairs of redox peaks at about 0.9/1.4 V and 1.3/1.7 V in RMBs, which represents the Li^+ insertion into/extraction from the CFS. Also, the voltage plateaus in the galvanostatic charge-discharge profiles of CFS in MLIBs at 100 mA g^{-1} (Figure S15) are coincident with the aforesaid CV results. Figure 5b displays semblable voltage plateaus and outstanding rate capability at different current densities. Benefiting from the insertion of Li^+ , the CFS electrodes in MLIBs show high discharge capacities of 611, 457, and 349.7 mAh g^{-1} at 100, 500, and 1000 mA g^{-1} (Figure S16, and Figure S17). More significantly, CFS shows an outstanding cycle stability with a high capacity retention of 87.6% (capacity decay rate of 0.16% per cycle) and Coulomb efficiency of over 99% at 3000 mA g^{-1} (Figure 5d). Besides, CFS also exhibits ultra-long lifespan at 2000 mA g^{-1} and remains a reversible capacity of 80 mAh g^{-1} after 14000 cycles (Figure S18). It is expressively superior compared to most of reported cathode materials (such as $\text{LiTi}_2(\text{PO}_4)_3$,^[56] MoS_2 ,^[57] V-doped Nb_2O_5 ,^[58] and others) for MLIBs in cycling number and capacity retention as shown in Figure 5c. As depicted in Figure 5e, GITT analysis was carried out to obtain the diffusion coefficients. The average diffusion coefficient of CFS in MLIBs ($1.5 \times 10^{-9} \text{ cm}^2 \text{s}^{-1}$) is about one order higher than which in RMBs.

3. Conclusions

In summary, CFS nanoparticles were successfully fabricated via a concise one-step hydrothermal method and firstly investigated as a cathode material for magnesium ion batteries. CFS

exhibits an excellent rate capability of 85 mAh g^{-1} at 1 A g^{-1} and exceptional long-term cycling stability of 86 mAh g^{-1} at 1 A g^{-1} after 600 cycles. The comprehensive mechanism investigation reveals a two-step reaction process for CFS cathode (solid solution reaction and conversion reaction process), and the conversion reaction occurs between $\text{Mg}_x\text{CuFeSe}_2$, Cu_2Se and metallic Fe^0 . Moreover, CFS electrode also displays splendid electrochemical performance in MLIBs with long cycling lifespan over 9500 cycles at 3000 mA g^{-1} and high stability (0.16% capacity decay per cycle). This work demonstrates CFS is a promising Mg-storage material and provides a prospective bimetallic strategy for advancing research on high-performance magnesium ion batteries.

Supporting Information

Supporting Information is available from the Wiley Online Library or from the author.

Acknowledgements

This work was supported by the National Key Research and Development Program of China (No. 2023YFB3809501), the National Natural Science Foundation of China (52172231), the Natural Science Foundation of Hubei Province (2022CFA087), the Fundamental Research Funds for the Central Universities (WUT: 2023-vb-004).

Conflict of Interests

The authors declare no conflict of interest.

Data Availability Statement

The data that support the findings of this study are available from the corresponding author upon reasonable request.

Keywords: transition metal selenides • magnesium-ion batteries • cathode material • CuFeSe₂

- [1] P. Zhou, M. Zhang, Q. H. Zhang, Z. Su, Y. Wang, X. Wang, Y. Hu, Y. Li, Z. Guo, *Mater. Lett.* **2020**, *273*, 127945.
- [2] W. Zhong, W. Tang, Y. Wu, Y. Zhang, Y. Qi, S.-j. Bao, X. Zhang, M. Xu, *J. Power Sources* **2021**, *506*, 230249.
- [3] G. Tian, G. Yuan, A. Aleksandrov, T. Zhang, Z. Li, A. M. Fathollahi-Fard, M. Ivanov, *Sustainable Energy Technol. Assess.* **2022**, *53*, 102447.
- [4] Y. Feng, L. M. Zhou, H. Ma, Z. H. Wu, Q. Zhao, H. X. Li, K. Zhang, J. Chen, *Energy Environ. Sci.* **2022**, *15*, 1711–1759.
- [5] M. Armand, J. M. Tarascon, *Nature* **2008**, *451*, 652–657.
- [6] B. Y. Liu, Q. Zhang, J. F. Liu, Y. W. Hao, Y. Y. Tang, Y. M. Li, *Energy* **2022**, *248*, 123646.
- [7] X. Wang, Z. Gu, E. H. Ang, X. Zhao, X. L. Wu, Y. Liu, *Interdiscip. Mater.* **2022**, *1*, 417–433.
- [8] K. V. Kravchyk, R. Widmer, R. Erni, R. J. C. Dubey, F. Krumeich, M. V. Kovalenko, M. I. Bodnarchuk, *Sci. Rep.* **2019**, *9*, 7988.
- [9] Z. Guo, S. Zhao, T. Li, D. Su, S. Guo, G. Wang, *Adv. Energy Mater.* **2020**, *10*, 1903591.
- [10] M. D. Regulacio, D.-T. Nguyen, R. Horia, Z. W. Seh, *Small* **2021**, *17*, 2007683.
- [11] H. D. Yoo, I. Shterenberg, Y. Gofer, G. Gershinsky, N. Pour, D. Aurbach, *Energy Environ. Sci.* **2013**, *6*, 2265–2279.
- [12] D. He, D. Wu, J. Gao, X. Wu, X. Zeng, W. Ding, *J. Power Sources* **2015**, *294*, 643–649.
- [13] F. Xiong, Y. Jiang, L. Cheng, R. Yu, S. Tan, C. Tang, C. Zuo, Q. An, Y. Zhao, J. J. Gaumet, *Interdiscip. Mater.* **2022**, *1*, 140–147.
- [14] X. Du, G. Huang, Y. Qin, L. Wang, *RSC Adv.* **2015**, *5*, 76352–76355.
- [15] Y. Xu, X. Deng, Q. Li, G. Zhang, F. Xiong, S. Tan, Q. Wei, J. Lu, J. Li, Q. An, L. Mai, *Chem* **2019**, *5*, 1194–1209.
- [16] C. Ling, R. G. Zhang, F. Mizuno, *ACS Appl. Mater. Interfaces* **2016**, *8*, 4508–4515.
- [17] W. X. Wang, Y. L. Jiang, Y. Yang, F. Y. Xiong, S. H. Zhu, J. J. Wang, L. L. Du, J. H. Chen, L. M. Cui, J. Xie, Q. Y. An, L. Q. Mai, *ACS Nano* **2022**, *16*, 17097–17106.
- [18] Q. Fu, R. Azmi, A. Sarapulova, D. Mikhailova, S. Dsoke, A. Missiul, V. Trouillet, M. Knapp, N. Bramnik, H. Ehrenberg, *Electrochim. Acta* **2018**, *277*, 20–29.
- [19] Y. Wang, X. Xue, P. Liu, C. Wang, X. Yi, Y. Hu, L. Ma, G. Zhu, R. Chen, T. Chen, J. Ma, J. Liu, Z. Jin, *ACS Nano* **2018**, *12*, 12492–12502.
- [20] M. Zhang, A. C. MacRae, H. Liu, Y. S. Meng, *J. Electrochem. Soc.* **2016**, *163*, A2368–A2370.
- [21] W. Li, M. Huang, Y. Li, C. Li, *Journal of Inorganic Materials* **2022**, *37*, 173–181.
- [22] Y. Shen, Y. Wang, Y. Miao, M. Yang, X. Zhao, X. Shen, *Adv. Mater.* **2020**, *32*, 1905524.
- [23] Z. Wang, S. Rafai, C. Qiao, J. Jia, Y. Zhu, X. Ma, C. Cao, *ACS Appl. Mater. Interfaces* **2019**, *11*, 7046–7054.
- [24] M. Wu, Y. Zhang, T. Li, Z. Chen, S.-a. Cao, F. Xu, *Nanoscale* **2018**, *10*, 12526–12534.
- [25] F. Xiong, Y. Fan, S. Tan, L. Zhou, Y. Xu, C. Pei, Q. An, L. Mai, *Nano Energy* **2018**, *47*, 210–216.
- [26] Y. Wang, Z. Liu, C. Wang, X. Yi, R. Chen, L. Ma, Y. Hu, G. Zhu, T. Chen, Z. Tie, J. Ma, J. Liu, Z. Jin, *Adv. Mater.* **2018**, *30*, 1802563.
- [27] C. Du, W. Younas, Z. Wang, X. Yang, E. Meng, L. Wang, J. Huang, X. Ma, Y. Zhu, C. Cao, *J. Mater. Chem. A* **2021**, *9*, 3648–3656.
- [28] S. Yang, F. Ji, Z. Wang, Y. Zhu, K. Hu, Y. Ouyang, R. Wang, X. Ma, C. Cao, *Electrochim. Acta* **2019**, *324*, 134864.
- [29] Y. Zhang, Y. Zhu, Z. Wang, H. Peng, X. Yang, Y. Cao, C. Du, X. Ma, C. Cao, *Adv. Funct. Mater.* **2021**, *31*, 2104730.
- [30] B. Liu, T. Luo, G. Mu, X. Wang, D. Chen, G. Shen, *ACS Nano* **2013**, *7*, 8051–8058.
- [31] Y. Gu, Y. Katsura, T. Yoshino, H. Takagi, K. Taniguchi, *Sci. Rep.* **2015**, *5*, 12486.
- [32] C. Li, W. Wu, Y. Liu, X. Yang, Z. Qin, Z. Jia, X. Sun, *J. Power Sources* **2022**, *520*, 230853.
- [33] Z. Li, J. Häcker, M. Fichtner, Z. Zhao-Karger, *Adv. Energy Mater.* **2023**, *2300682*.
- [34] L. C. Zeng, W. C. Zeng, Y. Jiang, X. Wei, W. H. Li, C. L. Yang, Y. W. Zhu, Y. Yu, *Adv. Energy Mater.* **2015**, *5*, 1401377.
- [35] P. Ge, C. Zhang, H. Hou, B. Wu, L. Zhou, S. Li, T. Wu, J. Hu, L. Mai, X. Ji, *Nano Energy* **2018**, *48*, 617–629.
- [36] M. L. Mao, T. Gao, S. Y. Hou, C. S. Wang, *Chem. Soc. Rev.* **2018**, *47*, 8804–8841.
- [37] Y. Tashiro, K. Taniguchi, H. Miyasaka, *Chem. Lett.* **2017**, *46*, 1240–1242.
- [38] Y. Tashiro, K. Taniguchi, H. Miyasaka, *Electrochim. Acta* **2016**, *210*, 655–661.
- [39] J. Zhang, Z. Chang, Z. Zhang, A. Du, S. Dong, Z. Li, G. Li, G. Cui, *ACS Nano* **2021**, *15*, 15594–15624.
- [40] Y. Zhang, T. Li, S.-a. Cao, W. Luo, F. Xu, *ACS Sustainable Chem. Eng.* **2020**, *8*, 2964–2972.
- [41] L. Zhou, F. Xiong, S. Tan, Q. An, Z. Wang, W. Yang, Z. Tao, Y. Yao, J. Chen, L. Mai, *Nano Energy* **2018**, *54*, 360–366.
- [42] Y. Ma, Y. Zhang, F. Wang, H. Xie, J. Wang, *Nanoscale* **2022**, *14*, 4753–4761.
- [43] X. Xue, R. Chen, X. Song, A. Tao, W. Yan, W. Kong, Z. Jin, *Adv. Funct. Mater.* **2021**, *31*, 2009394.
- [44] D. Chen, Y. Zhang, X. Li, J. Shen, Z. Chen, S.-a. Cao, T. Li, F. Xu, *Nanoscale* **2019**, *11*, 23173–23181.
- [45] X. Xue, X. Song, W. Yan, M. Jiang, F. Li, X. L. Zhang, Z. Tie, Z. Jin, *ACS Appl. Mater. Interfaces* **2022**, *14*, 48734–48742.
- [46] Y. Cao, Y. Zhu, C. Du, X. Yang, T. Xia, X. Ma, C. Cao, *ACS Nano* **2022**, *16*, 1578–1588.
- [47] Y. Zhang, J. M. Cao, Z. Yuan, H. Xu, D. Li, Y. Li, W. Han, L. Wang, *Small* **2022**, *18*, 2202313.
- [48] Y. Miao, X. Xue, Y. Wang, M. Shi, H. Tang, T. Huang, S. Liu, M. Zhang, Q. Meng, J. Qi, *ACS Appl. Mater. Interfaces* **2023**, *15*, 57079–57087.
- [49] V. Augustyn, J. Come, M. A. Lowe, J. W. Kim, P. L. Taberna, S. H. Tolbert, H. D. Abruna, P. Simon, B. Dunn, *Nat. Mater.* **2013**, *12*, 518–522.
- [50] J. Wang, J. Polleux, J. Lim, B. Dunn, *J. Phys. Chem. C* **2007**, *111*, 14925–14931.
- [51] C. Choi, D. S. Ashby, D. M. Butts, R. H. DeBlock, Q. L. Wei, J. Lau, B. Dunn, *Nat. Rev. Mater.* **2020**, *5*, 5–19.
- [52] X. Yu, G. Zhao, C. Wu, H. Huang, C. Liu, X. Shen, M. Wang, X. Bai, N. Zhang, *J. Mater. Chem. A* **2021**, *9*, 23276–23285.
- [53] A. Roy, M. Sotoudeh, S. Dinda, Y. Tang, C. Kübel, A. Groß, Z. Zhao-Karger, M. Fichtner, Z. Li, *Nat. Commun.* **2024**, *15*, 492.
- [54] D. Ni, J. Shi, W. Xiong, S. Zhong, B. Xu, C. Ouyang, *Phys. Chem. Chem. Phys.* **2019**, *21*, 7406–7411.
- [55] Y. Wang, C. Wang, X. Yi, Y. Hu, L. Wang, L. Ma, G. Zhu, T. Chen, Z. Jin, *Energy Storage Mater.* **2019**, *23*, 741–748.
- [56] Y. N. Xu, C. Xu, Q. Y. An, Q. L. Wei, J. Z. Sheng, F. Y. Xiong, C. Y. Pei, L. Q. Mai, *J. Mater. Chem. A* **2017**, *5*, 13950–13956.
- [57] X. B. Yu, G. Y. Zhao, C. Liu, C. L. Wu, H. H. Huang, J. J. He, N. Q. Zhang, *Adv. Funct. Mater.* **2021**, *31*, 2103214.
- [58] H. H. Huang, G. Y. Zhao, X. B. Yu, X. J. Shen, M. Wang, X. M. Bai, N. Q. Zhang, *J. Mater. Chem. A* **2022**, *10*, 577–584.

Manuscript received: January 26, 2024

Revised manuscript received: March 20, 2024

Accepted manuscript online: April 4, 2024

Version of record online: May 2, 2024